

One-Step Synthesis and Deposition of Metal Oxides: NiO Quantum Dots as a Transport Layer for Perovskite Photovoltaics

Dilli babu Padmanaban, Subha Sadhu, Slavia Deeksha Dsouza, Warda Mushtaq, Zachary Holman, Vladimir Svrcek, and Davide Mariotti*

One-step synthesis and deposition of nickel oxide quantum dots using a gas-phase microplasma process is demonstrated and their applicability as a transport layer for solar cell devices is shown. The process uses a solid nickel metal wire as sacrificial electrode, and the concentration of oxygen gas required in the synthesis is investigated. The quantum dots are characterized for physical, chemical, and optical properties and critical process parameters such as the process throughput are also estimated. Direct one-step deposition directly on perovskite solar cells is carried out using a computer-controlled x-y stage and the performance of the solar cell device is assessed.

1. Introduction

Metal oxides exhibit important optical and electrical properties highly relevant for many application devices such as sensors,


D. Padmanaban, S. Sadhu, S. D. Dsouza
Plasma Science and Nanoscale Engineering Group
Ulster University
Belfast BT15 1AP, UK

S. Sadhu
Department of Chemistry
Institute of Science
Banaras Hindu University
Varanasi 221005, India

W. Mushtaq, Z. Holman
School of Electrical, Computer, and Energy Engineering
Arizona State University
Tempe, AZ 85287-5706, USA

V. Svrcek
National Institute of Advanced Industrial Science and Technology (AIST)
Central 2
Umezono 1-1-1, Tsukuba, Ibaraki 305-8568, Japan

D. Mariotti
Department of Design, Manufacturing and Management Engineering
University of Strathclyde
Glasgow G1 1XJ, UK
E-mail: davide.mariotti@strath.ac.uk

 The ORCID identification number(s) for the author(s) of this article can be found under <https://doi.org/10.1002/adem.202400826>.

© 2024 The Authors. Advanced Engineering Materials published by Wiley-VCH GmbH. This is an open access article under the terms of the Creative Commons Attribution License, which permits use, distribution and reproduction in any medium, provided the original work is properly cited.

DOI: 10.1002/adem.202400826

flat panel displays, photovoltaic (PV) cells, etc.^[1] For instance, their wide bandgap and transparency offer excellent opportunities for PV devices and for the development of second- and third-generation solar cells including organic, dye-sensitized, quantum dot (QD), and organohalide perovskite solar cells (PSCs),^[2–6] where metal oxides are extensively employed as charge extraction/transport layers. For instance, PSCs strongly rely on the performance of their electron transport layer (ETL) and hole transport layer (HTL), including their optical transparency, depending on the config-

uration (e.g., inverted). TiO₂, ZnO, and SnO₂ are commonly used as ETLs in perovskite devices either as thin films, nanostructured, or as a combination forming a mesoporous structure.^[7] Organic compounds such as 2,2',7,7'-tetrakis (N,N-di-*p*-methoxyphenylamine)-9, 9'-spirobifluorene (spiro-OMeTAD), poly (3,4-ethyl-enedioxythiophene):poly(4-styrenesulfonate) (PEDOT:PSS) and Poly(N,N'-bis(4-butylphenyl)-N,N'-bis(phenyl)benzidine) (Poly-TPD) are generally used as HTLs.^[8,9] However, organic HTL have some disadvantages due to their relatively poor stability and unmatched energy band levels as well as limited deposition scalability and high costs. For these reasons, suitable metal oxides are also being investigated as HTLs (e.g., NiO_x, Cu_xO, CrO_x, VO_x, and MoO_x).^[2,10–12]

Nickel oxides are transition metal oxides that are used in several applications such as in catalysis,^[13] gas sensors,^[14] optoelectronic devices,^[15] energy conversion,^[14] and memory storage.^[16] They have a wide bandgap ranging from 3.6 to 4.3 eV and a well-known p-type semiconductor behavior due to its intrinsic oxygen-rich and nickel-deficient nature. Stoichiometric NiO phase relates to nickel in its +2 state, and it exhibits a cubic rock salt crystal structure. Nickel oxides with a +3 oxidation state (Ni₂O₃) or as an oxy-hydroxy phase (NiOOH) have been also reported and used in many optoelectronic applications.^[7,17,18] While wet chemistry approaches have been often used, plasma-based synthesis methods offer advantages and opportunities. In particular, microplasmas operated at atmospheric pressure have shown substantial capability for nanomaterials synthesis.^[19–26]

In particular we have previously synthesized NiO QDs using plasma-induced nonequilibrium electrochemistry,^[27] which however produces colloids and cannot be directly deposited as films.

Here we report for the first time a one-step synthesis and deposition of NiO QDs using atmospheric pressure microplasma

synthesis. Compared to other approaches,^[28–32] this methodology uses a simple solid metal and gaseous molecular oxygen as precursor, eliminating the need for complex and costly chemical compounds that are required in other synthesis techniques to be used as precursors, reducing agents, and surfactants. This microplasma process therefore eliminates all purification steps, minimizing waste and maximizing yield. The process is scalable and applicable to a very wide range of other metal and metal oxides (e.g., Au, W, Mo, Zn, Cu).^[19,20,23,24,33–41] We demonstrate here that the synthesis of NiO is also achievable and that ultra-small QDs can be produced, adding opportunities for customizing band energy-level alignment.

2. Results and Discussion

2.1. System Configuration

The synthesis setup (Figure 1) consists of a microplasma reactor with two ceramic tubes placed coaxially in which the inner tube (1.3 mm outer diameter, 0.7 mm inner diameter) contains a 0.5 mm-diameter nickel wire (99.99% purity, purchased from Alfa Aesar), whereas the outer ceramic tube (3 mm outer diameter, 2 mm inner diameter) carries the process gases. Both tubes are inserted into two parallel copper electrodes, both powered by a radio frequency (RF; 13.56 MHz) power supply (Figure 1b). All the components are held together with a Perspex frame. The deposition processes were carried out for different oxygen

Table 1. Process parameters for nickel oxide deposition.

He gas [sccm]	O ₂ gas [sccm]	O ₂ gas fraction [%]
500	56	10
500	113	18
500	168	25
500	224	31

concentrations with constant He gas flow of 500 sccm, 70 W RF power, as shown in Table 1. The process was used to deposit films of NiO QDs directly on various solid substrates. Unless otherwise stated, the entire process was carried out for a duration of 2 min with a working distance of 7 mm between the tip of the outer capillary and the substrate.

2.2. Material Characterization of the NiO QDs and Corresponding Films

Figure 2a–c shows low- and high-resolution transmission electron microscopy (TEM) images as well as size distribution analysis for the samples produced with 31% oxygen. Synthesis at other oxygen concentrations produced similar results (see Figure S1a–c, Supporting Information). The TEM analysis shows the presence of well-defined crystallites with sizes varying within the range 1–6 nm. The size distribution of the crystallites for different

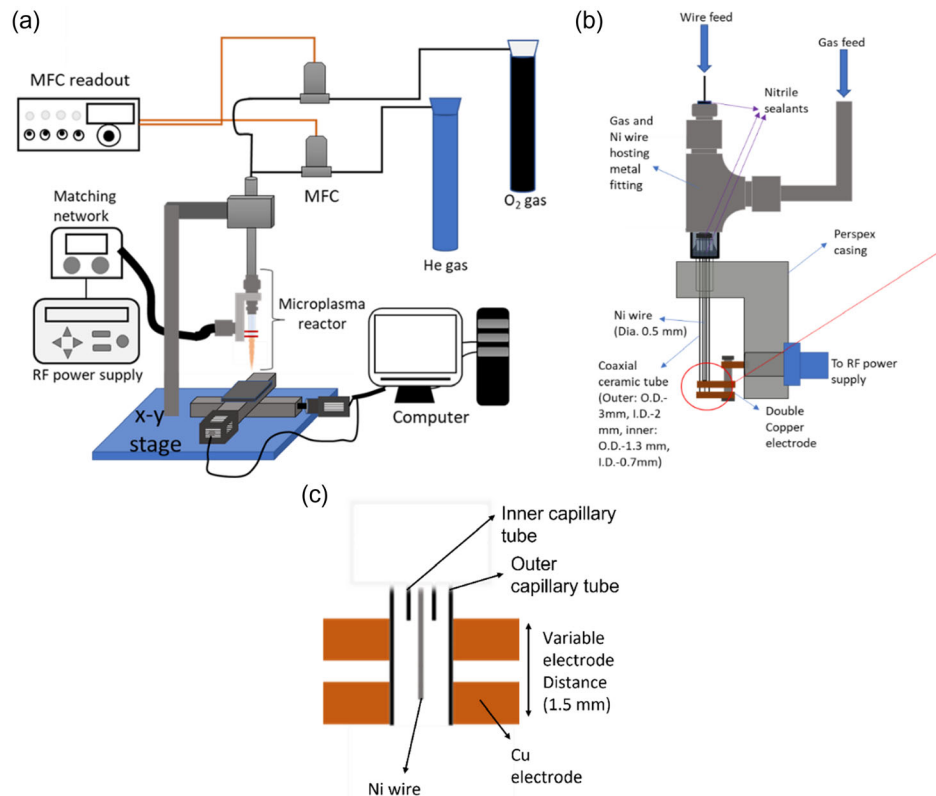


Figure 1. a) Schematic of the full microplasma deposition system and b) microplasma reactor used for nickel oxide deposition. c) Enlarged part of electrodes region with Ni wire inside the capillary tubes.

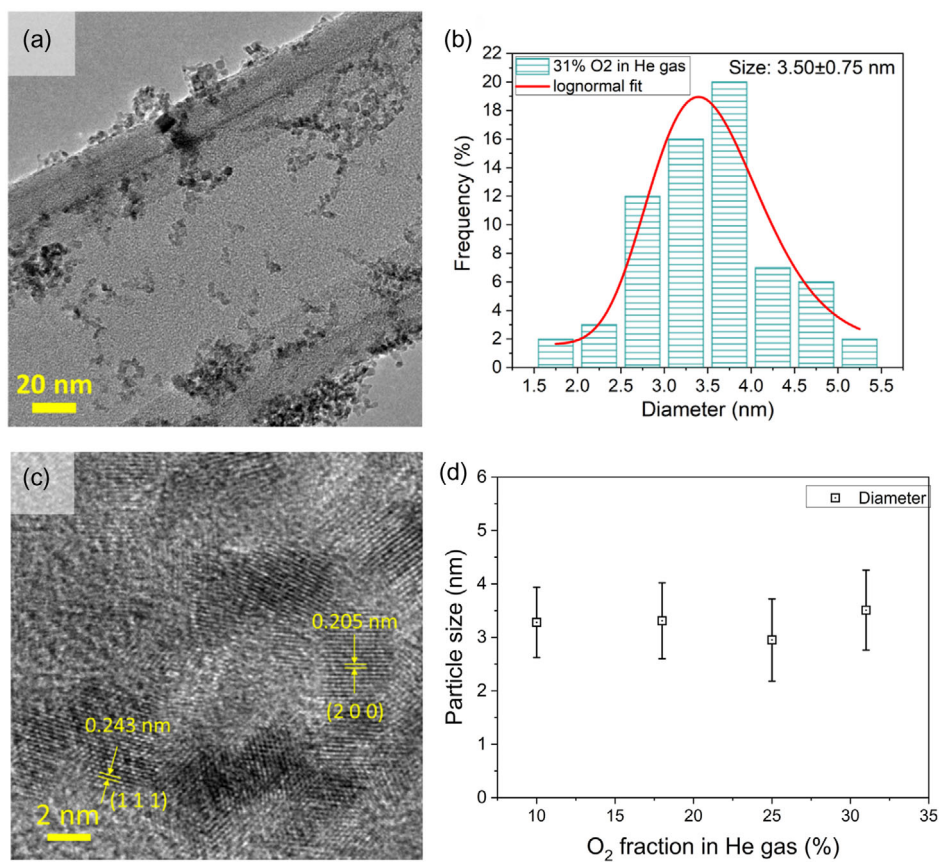


Figure 2. a) Transmission electron micrograph, b) size distribution, and c) high resolution with lattice fringes of QDs obtained for 31% oxygen gas fractions. d) Size variation of QDs for different oxygen gas fractions with error bar representing the standard deviation from lognormal size distribution.

oxygen gas mixing fractions is summarized in Figure 2d with mean sizes varying between 2.9 and 3.5 nm. In the high-resolution images, clear fringe patterns can be observed. Lattice spacing with values of 0.205–0.208 and 0.239–0.243 nm could be found, which correspond to the most prominent lattice planes related to the (200) and (111) planes of the NiO cubic phase with values of 0.209 and 0.242 nm respectively. The TEM analysis therefore suggests that quantum confined crystallites have been produced (i.e., QDs, NiO Bohr radius is 7.7 nm)^[42] and that the crystal structure is consistent with that of the rock-salt (Bunsenite) phase of (NiO) nickel oxide.

Figure 3 presents the scanning electron microscopy (SEM) images of QD films deposited on Si substrates with the insets showing the cross section of the films. The films were synthesized for different oxygen gas concentrations (Table 1), and they reveal both smooth-to-rough features also with columnar structures. The films appear compact for lower oxygen concentrations and the thickness increases with increasing O₂ gas fraction, as presented in Figure 4.

Figure 5 presents the grazing-incidence X-ray diffraction (GIXRD) of the NiO QDs on Si substrates. All the samples show a well-defined diffraction pattern with broad peaks, which were further compared with peaks from standard JCPDS (file# 780429 for NiO, pdf#140481 for Ni₂O₃, pdf#270956 for NiOOH, and pdf#731520 for Ni(OH)₂) for possible existence of nickel oxides.

Also, in this case, the diffraction patterns from samples produced with a higher content of oxygen in the process gases show a similar crystal structure. The peaks match with the cubic rock-salt phase of nickel oxide (NiO) corresponding to the (111), (200), and (220) crystal planes. The peaks are broad, as expected for crystallites of the dimensions observed by TEM. We should also note that the peak above 35° is shifted with respect to the reference and we attribute this to the lattice relaxation of the QD sized NiO particle as compared to referenced bulk nickel oxide.^[43] However, the spectra of NiO QDs produced with only 10% oxygen gas confirm incomplete oxidation as, in addition to NiO peaks, peaks could also be matched with peaks belonging to the crystal planes (121) and (220) from the NiOOH phase (74.08° and 75.39°).

Overall, the material characterization indicates the formation of NiO quantum confined crystallites (<5 nm diameter) with nonstoichiometric or partial oxidation at the surface. The use of different oxygen concentration in the process gas does not appear to impact the morphology; however, it is clear that a supply of low oxygen influences the oxidation process and reduces the NiO crystal phase.

The chemical composition of the QD films was characterized using X-ray photoelectron spectroscopy (XPS). Figure 6 shows the elemental content of the film measured from the survey spectra (shown in Figure S2a, Supporting Information), which

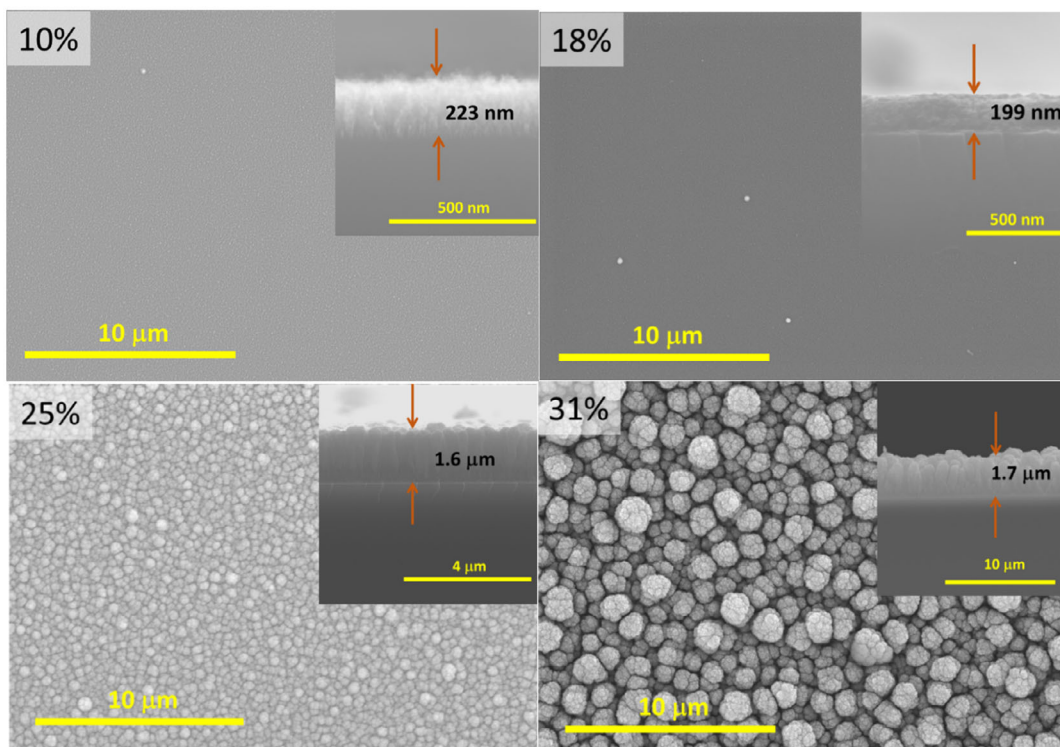


Figure 3. Film morphology after deposited at static condition for various O₂ gas fraction.

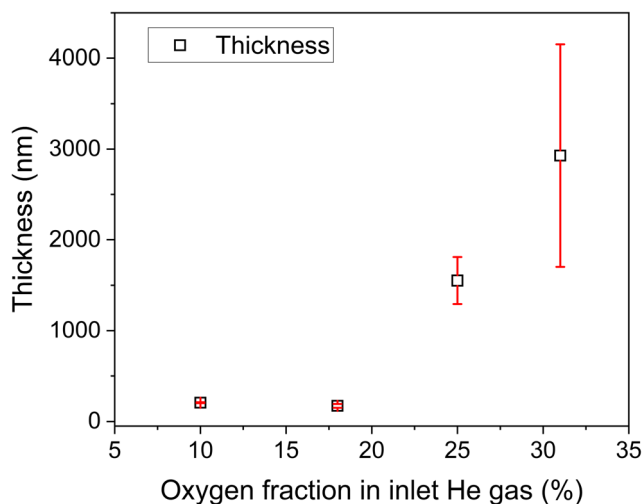


Figure 4. Variation in cross-sectional thickness of the films on Si substrate deposited at static condition with error bar representing the standard deviation estimated from ~35 thickness measurements across the substrate.

include nickel and oxygen as expected and carbon from environmental contamination as it is normally observed. The atomic percentage of Ni and O is shown in Figure 6a. The oxygen content in the samples is impacted by environmental contamination; hence, these results cannot contribute to defining the stoichiometry of the NiO QDs; however, these results show that the concentration of oxygen in the process gas has negligible impact in the

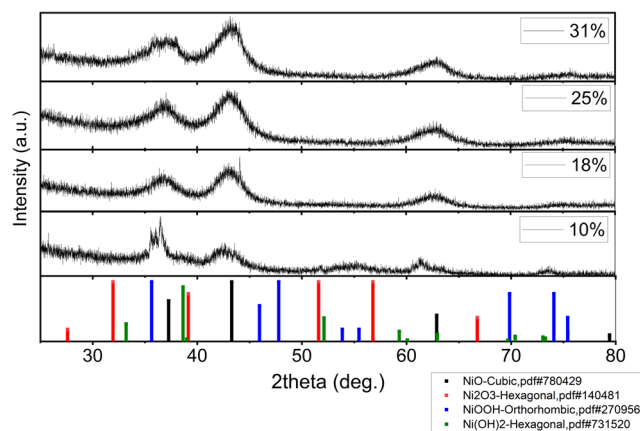


Figure 5. X-ray diffractogram of nanoparticle film on Si substrate for different oxygen gas mixing with various standard JCPDF nickel oxide phases.

chemical composition. The chemical oxidation states of nickel and oxygen were therefore explored through their high-resolution scans (see Supporting Information which includes full details on deconvolution). We have identified a component at 854.7 eV that belongs to the NiO phase^[44] or presence of Ni²⁺ state and the second component around 855.5 eV is identified to belong to Ni(OH)₂,^[45] Ni₂O₃,^[46] or β, γ-NiOOH^[47] phases, which are likely due to surface states of the QDs. The profile also includes a higher-energy broad component approximately around 857 eV assigned to a loss process due to the presence

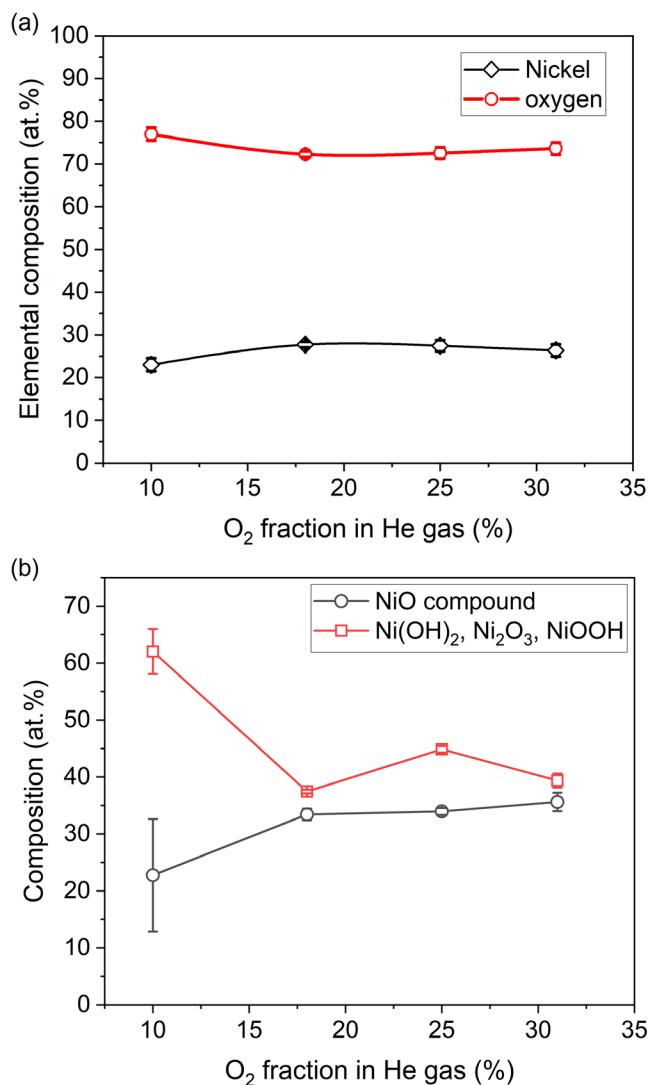


Figure 6. a) Elemental quantification of nanoparticle film on Au-coated Si substrate and b) surface chemical composition film using Ni 2p.

of NiOOH in the film as reported.^[48] Figure 6b shows the estimates of these nickel oxidation states/phases for different oxygen gas fractions. When more than 15% oxygen is used in the process gas, the chemical composition of the NiO QDs is similar with a constant fraction of the NiO phase, that is, Ni²⁺ state. Surface and other states are also relatively constant, however with some minor fluctuations at 25% oxygen. At low oxygen concentration in the process gas (10%), the NiO phase concentration is lower than for NiO QDs produced at higher oxygen concentrations. Correspondingly the oxidation states related to nonstoichiometric NiO are higher in percentage and suggest incomplete oxidation. The presence of the NiOOH phase is reported to originate from oxidation of NiO in the presence of water and from oxygen species,^[49] consistent with higher density of surface states and partial oxidation at low oxygen gas concentration and where humidity from ambient air may have contributed to different oxidation paths.

2.3. Energy Band Analysis

Figure 7a presents the optical transmittance of the films. The samples obtained with different oxygen gas mixtures show transparency over visible light with a strong absorption in the ultraviolet (UV) region. The bandgap values were also estimated (Figure 7b, see also Supporting Information). Several earlier works have reported that nickel oxide compounds behave as a direct-bandgap material with values ranging from 3.4 to 4.8 eV.^[50,51] The values measured here are similar for all synthesis conditions and range within 3.6 and 3.8 eV, in agreement with expected values.^[52]

The work function of the NiO QDs films on gold-coated silicon substrates was measured by Kelvin probe microscopy. The measurements are performed with a calibrated Au-alloyed tip work function. Figure 8a presents the work function 2D area map of NiO film obtained for 31% oxygen fraction. The work function of the films for different oxygen gas fractions was measured in

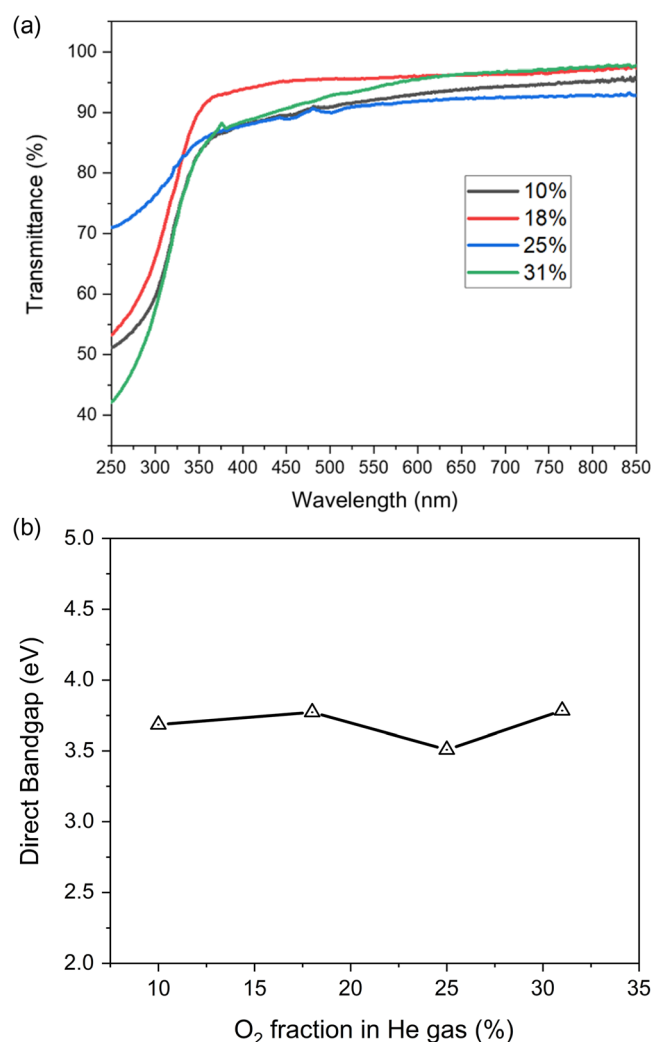


Figure 7. Optical characteristics of nickel oxide film on quartz substrate. a) Variation of light transmittance and b) estimated bandgap for different oxygen gas mixture.

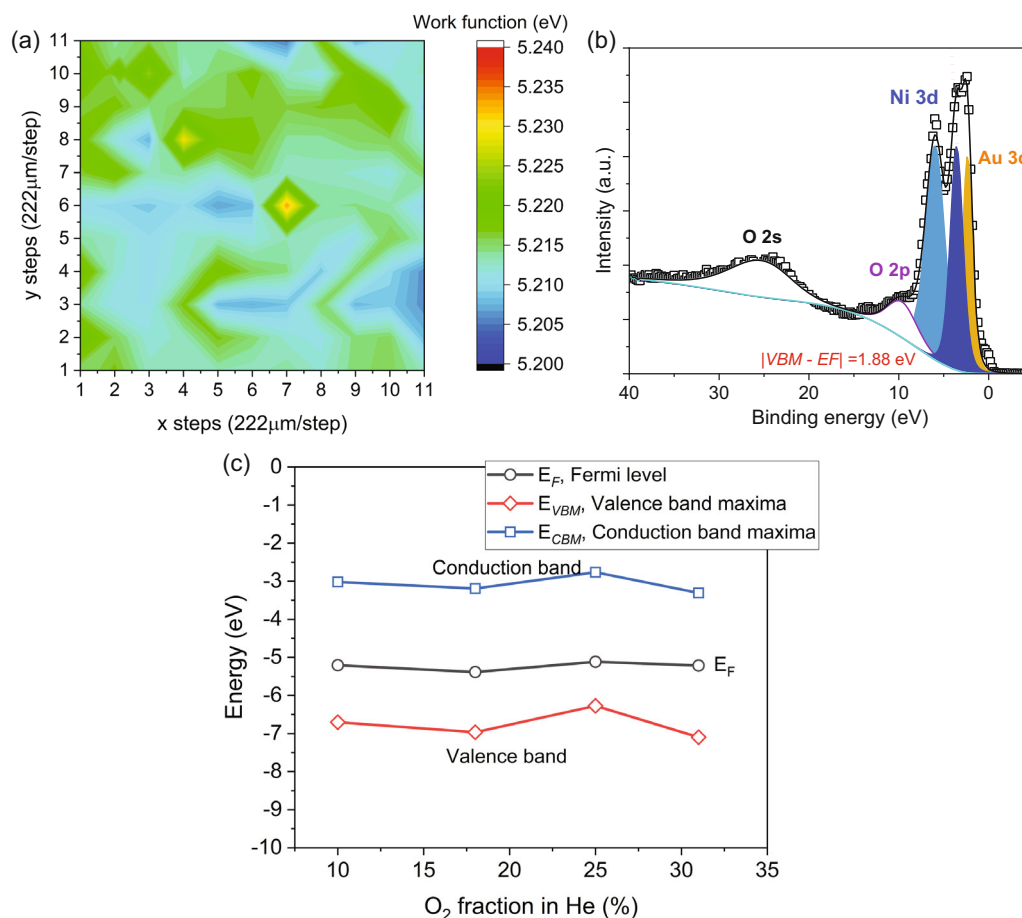


Figure 8. Energy band analysis of NiO nanoparticles: a) work function, b) XPS valence band spectra of NiO obtained at 31% oxygen gas mixing, and c) complete energy band diagram of NiO nanoparticle obtained at different oxygen fractions.

the range 5.1–5.4 eV (see Supporting Information), which is close to the value reported in the literature (≈ 5.3 eV).^[53,54] However, other values that varied from 4.8 to 5.6 eV and even 6.4 eV have been also reported depending on the crystal planes and surface chemistry.^[55,56] Figure 8b shows the XPS valence band spectra of NiO film produced with 31% oxygen on gold-coated Si substrate, revealing valence orbital of metal Ni 3d and oxygen O 2p levels along with Au 3d from the Au film (see Supporting Information for XPS valence band measurements at other synthesis conditions). The difference between the valence band maximum edge and the Fermi level (E_F) was estimated from the Ni 3d level after deconvolution (Figure 8b) and produced a value of 1.88 eV. Figure 8c shows the overall energy band diagram determined from work function, XPS valence band, and transmission measurements.

While the oxygen concentration used in the process gas affected surface states of the NiO QDs, this does not appear to impact the optoelectronic properties dramatically. The band diagram shows some changes at 25% oxygen; however, these are still relatively small. These measurements confirm the quantum confinement regime of the NiO crystallites and its slightly ‘p-type’ behavior.

2.4. Process Characterization

As low oxygen concentration in the process gas impacts the crystal structure of the NiO QDs and a higher concentration appears to increase the throughput (e.g., Figure 3), we further analyzed the synthesis with 31% oxygen. The mass deposited by the process was measured with the quartz crystal microbalance (QCM) and the results are reported in Figure 9 (see supporting information for more results). The mass deposited increases very quickly in the first ≈ 1 min of the process reaching ≈ 4.3 μg and subsequently deposition appears to stop. We believe that this is due to the Ni wire consumption; hence, it suggests that a wire feeding apparatus would be required for a continuous deposition.

We have then carried out experiments to further assess the film deposition and corresponding thickness with an x - y motorized stage. The schematic of the setup is shown in Figure S6 in the Supporting Information. As we are currently limited by the wire consumption speed, the deposition was carried out with 20 mm-long linear scans at speeds of 25 and 100 mm s^{-1} and for different number of scans. The thickness was studied by cross-sectional SEM analysis (see supporting information for images) on Si- and Au-coated Si substrates because we observed

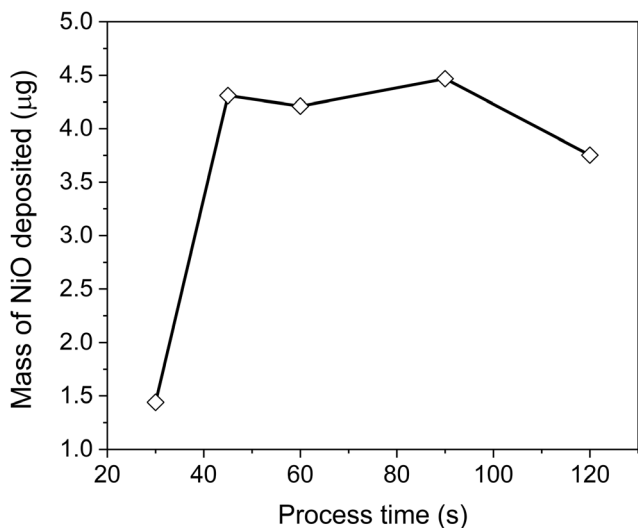


Figure 9. Estimation of mass of NiO deposition at 31% oxygen gas mixing for different process times.

different deposition rates for different substrates (**Figure 10**). Deposition at 25 mm s^{-1} (Figure 10a) shows an almost linear trend with time/number of scans. However, the thickness is higher when deposition is carried out on silicon substrates. Various factors can play a role in this result. For instance, QDs are expected to be negatively charged when they exit the plasma, and the substrate conductivity/charging state may impact both the collection efficiency of the QDs and the compactness or porosity of the film. The values of thickness observed are relatively high and for many applications much thinner films are often required. We have therefore characterized the deposition at a higher scan speed, 100 mm s^{-1} .

The results at higher speed show similar linear trends with deposition on silicon, also presenting higher thickness values. Thinner films are also achievable, increasing the deposition speed; however, porosity and roughness (Figure S8 in Supporting Information) become more prominent (see Supporting Information for ellipsometry results in Table S2).

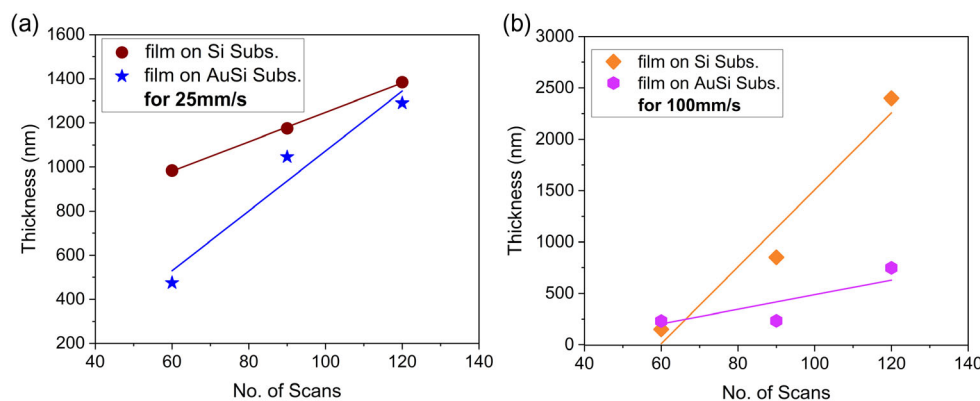


Figure 10. NiO film thickness optimization for different scan numbers with a) 25 and b) 100 mm s^{-1} scan speeds performed on silicon- and gold-coated silicon substrates.

2.5. Application of NiO Hole Transport Layer for Solar Cells

As a final assessment for this deposition technique, we have fabricated solar cell devices, using the NiO QD film as HTL directly deposited over the active layer of methyl ammonium lead iodide (MAPI) perovskite (see Supporting Information on the device fabrication). We have chosen MAPI-based devices due their current relevance in PVs and because new approaches for transport layers are currently needed for these types of devices to prevent or limit the perovskite decomposition at ambient conditions. Additive-free, cost-effective, stable HTLs are required to replace expensive organic HTLs. Moreover, for organic HTLs, conducting enhancing additives are required which make the fabrication process more laborious and time consuming. Hence a one-step deposition of stable NiO QDs on top of the perovskite layer can be an ideal step for device fabrication.

NiO QDs were deposited on top of the perovskite layer using gas-phase microplasma at process condition of 31% O_2 mixing for a total duration of 1 min. The deposition required is in this case over an active area of $25 \text{ mm} \times 13 \text{ mm}$. The moving stage was programmed to scan for a length of 35 mm, that is, exceeding the device length by 5 mm on each side of the required deposition area. A speed of 100 mm s^{-1} was selected, and deposition was carried out for 52 scans. The distance between the microplasma capillary and the surface of the device was set at 15 mm. **Figure 11** presents the current density–voltage (J – V) curve of the device with/without NiO QDs as HTL layered device. As this is a proof of principle study for the deposition methodology, devices are not optimized and produced in open air, which limit their overall performance. Hence, the most important result here is that the deposition has not damaged the underlying layer and the device is still in working conditions with good rectification (Figure 11); this is also important in the context of the perovskite degradation considering that oxygen was included in the process gas. Further we observed an improvement in the overall efficiency with the NiO QDs, from 1.8% to 2.8%, as it would be expected by adding the HTL. After the deposition of the HTL, the current density increases from 3.85 to 6.09 mA cm^{-2} whereas there is no significant change in open-circuit voltage. This suggests the effectiveness of NiO as HTL

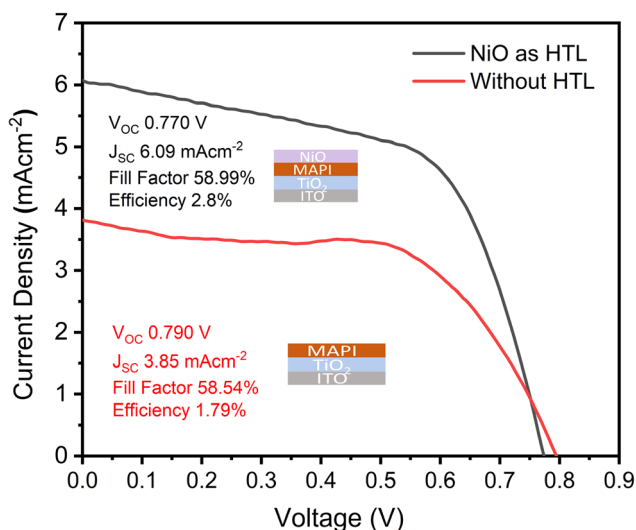


Figure 11. *I*–*V* characteristics of NiO nanoparticle HTL with MAPI solar cell device with insets showing the device performance and architectures.

to enhance charge transport and confirms the viability of this microplasma-based one-step synthesis and deposition of NiO QDs films.

3. Conclusion

NiO QD synthesis (2–4 nm) was demonstrated using a gas-phase microplasma process using a sacrificial Ni wire electrode and oxygen gas as precursor. The process was investigated for different oxygen gas concentrations, revealing that this parameter has limited impact on the synthesis process for the range of concentrations considered. The analysis of the deposition process suggests that very fast deposition can be achieved, in particular for thin films (<500 nm). However, further work will be required to understand on how to control roughness and porosity. For large-area deposition, the process can be scaled up by producing arrays where continuous wire feeding would also be required. One of the most important aspects of this technology is the real possibility of generalizing the process for a very wide range of metal oxides.

4. Experimental Section

Material Characterization: The film morphology was analyzed using field-emission SEM (FESEM) with a Hitachi SU5000 operated at a potential of 15 kV and emission current of 0.215 mA in observation mode. Images were captured for different magnifications with a fixed working distance of 5 mm. For the measurements, the samples were prepared by depositing the QDs onto Si substrate in static condition, that is, without changing the relative position of the substrate with respect to the microplasma. Energy-dispersive X-ray analysis on different spots on the samples were measured using air-cooled X-Max^N 80 silicon drift detector coupled with FESEM system operated via AZtech 3.3 software from oxford instruments nanotechnology Tools Ltd. with the same accelerating voltage and current as used for microscopy imaging.

The optical characteristics of the QDs films were characterized using a Perkin Elmer-Lambda 1050+ spectrometer. Also, in this case,

the samples were produced by depositing on quartz substrate in static conditions for different oxygen gas mixing. The optical transmittance (*T*) of the films was recorded in the transmittance compartment and the corresponding absorption coefficients (α) were estimated (see Supporting Information).

The crystal structure and morphology of the NiO QDs were studied using TEM (JOEL, JEM-2100F with a Gatan DualVision 600 charge-coupled device) at an accelerating voltage of 200 kV. For TEM measurements, all the samples were prepared initially by depositing onto n-type Si substrate, then scratched, and redispersed as a colloid in ethanol (purity 99.8%, Sigma Aldrich). 20 μ L of the colloid in ethanol was drop cast onto a holey carbon-coated grid (400 mesh, #S187-4, Agar Scientific) with an ultrathin carbon film (3 nm thick) and allowed to dry completely under ambient conditions leaving the grids overnight. The d-spacing values of the crystal planes were measured on the digital image using ImageJ software.

GIXRD measurements were carried out using an EMPYREAN PANalytical instrument with monochromatic Cu K α X-ray (wavelength = 1.5406 Å) radiation generated at an accelerating voltage of 45 kV and a current of 40 mA. The incidence angle for all measurements was set within the range 0.3°–0.5° with respect to the sample plane and data were acquired at a rate of 0.0065° increments with a scan speed of 300 and 500 s per step. Finally, the phases in the samples were identified using the standard JCPDF files obtained from international centre for diffraction data database.

XPS was performed by direct deposition of NiO QDs on gold-coated silicon substrates. Analysis was performed using an ESCALAB Xi+ spectrometer microprobe (Thermo Fisher Scientific) with a focused monochromatic Al K α X-ray source ($h\nu = 1486.6$ eV, 650 μ m spot size) operating at a power of 225 W (15 kV and 15 mA), and the photoelectrons were collected using a 180° double-focusing hemispherical analyzer with a dual-detector system. The energy scale of spectrometer was calibrated with sputter-cleaned pure reference samples Au, Ag, and Cu (Au 4f_{7/2}, Ag 3d_{5/2}, and Cu 3p_{3/2}) positioned at binding energies of 83.96, 368.21, and 932.62 eV, respectively. The base pressure in the analysis chamber was better than 5×10^{-9} mbar, which increased up to 5×10^{-7} mbar with charge neutralizer (flood gun) operated at 100 μ A emission current. For the Fermi-level alignment, a copper strip was used to make good electrical contact between the sample and the spectrometer. For all the samples analyzed, the survey spectra were recorded with a step size of 1 eV and a pass energy of 150 eV and the narrow scans were recorded with a step size of 0.1 eV and a pass energy of 20 eV. This pass energy gave 0.65 eV width for the Ag 3d_{5/2} peak measured on a sputter-cleaned Ag sample. The spectra obtained were charge corrected using Au core level and valence band spectra.

Mass of NiO QDs deposition was studied using QCM. The setup consisted of rate monitor SQM 160 from Sigma instruments along with oscillator bridge and quartz sensor. The sensor hosted 10 mm-diameter gold-coated quartz crystal (frequency = 6 MHz) with a 6 mm-diameter window for deposition. The measurement was performed by first recording the change in frequency in the interval of every 30 up to 120 s and using Sauerbrey equation; the mass NiO QD deposition was estimated and presented. For this, the plasma was operated at RF power of 70 W with 31% O₂ gas mixture in 500 sccm He gas.

The temperature of the NiO deposition process on the substrate was measured using a noncontact infrared pyrometric technique using the device thermoMETER CT from Micro-Epsilon UK Ltd. with temperature range from –50 to 1600 °C. For this measurement, the process was performed at 70 W RF power with 31% oxygen gas fraction in 500 sccm He gas. The IR temperature probe was placed at a distance of 15 mm, angle of 45° from the substrate. The sample also maintained was kept at a distance of 15 mm from the plasma with sample area of 10 \times 10 mm² monitored for temperature change.

Current–voltages (*J*–*V*) of MAPI/NiO device were characterized by irradiating the cell with 100 mW cm^{–2} (450 W xenon lamp, Oriel instrument). A 1 sun AM1.5G filter was used to simulate the solar spectrum. The active area of the cell was 1 mm². The photocurrent was measured using a Keithley 2400 source measure unit.

Supporting Information

Supporting Information is available from the Wiley Online Library or from the author.

Acknowledgements

This work was supported by EPSRC (EP/V055232/1, EP/R008841/1, EP/M024938/1) and by the Japan Society for the Promotion of Science through the Invitational Fellowships for Research in Japan 2022.

Conflict of Interest

The authors declare no conflict of interest.

Data Availability Statement

The data that support the findings of this study are available from the corresponding author upon reasonable request.

Keywords

manufacturing, photovoltaics, plasmas, quantum dots, transport layers

Received: April 12, 2024

Published online:

- [1] D. S. Ginley, J. D. Perkins, in *Handbook of Transparent Conductors* (Ed: D. S. Ginley), Springer, Boston, MA **2011**.
- [2] M. A. Haque, A. D. Sheikh, X. Guan, T. Wu, *Adv. Energy Mater.* **2017**, 7, 1602803.
- [3] R. Jose, V. Thavasi, S. Ramakrishna, *J. Am. Ceram. Soc.* **2009**, 92, 289.
- [4] J. M. Caruge, J. E. Halpert, V. Wood, V. Bulović, M. G. Bawendi, *Nat. Photonics* **2008**, 2, 247.
- [5] National Renewable Energy Laboratory, Best Research-Cell Efficiency Chart **2023**.
- [6] Y. Li, R. L. Z. Hoye, H.-H. Gao, L. Yan, X. Zhang, Y. Zhou, J. L. MacManus-Driscoll, J. Gan, *ACS Appl. Mater. Interfaces* **2020**, 12, 7135.
- [7] H. Park, R. Chaurasiya, B. H. Jeong, P. Sakthivel, H. J. Park, *Adv. Photonics Res.* **2021**, 2, 2000178.
- [8] M. Jeong, I. W. Choi, E. M. Go, Y. Cho, M. Kim, B. Lee, S. Jeong, Y. Jo, H. W. Choi, J. Lee, J.-H. Bae, S. K. Kwak, D. S. Kim, C. Yang, *Science* **2020**, 369, 1615.
- [9] Y. Yao, C. Cheng, C. Zhang, H. Hu, K. Wang, S. De Wolf, *Adv. Mater.* **2022**, 34, 2203794.
- [10] Q. Wang, Z. Lin, J. Su, Z. Hu, J. Chang, Y. Hao, *Nano Sel.* **2021**, 2, 1055.
- [11] S. Li, Y. L. Cao, W. H. Li, Z. S. Bo, *Rare Met.* **2021**, 40, 2712.
- [12] X. Yin, Y. Guo, H. Xie, W. Que, L. B. Kong, *Sol. RRL* **2019**, 3, 1900001.
- [13] A. Singh, S. L. Y. Chang, R. K. Hocking, U. Bach, L. Spiccia, *Energy Environ. Sci.* **2013**, 6, 579.
- [14] I. Hotovy, J. Huran, L. Spiess, S. Hascik, V. Rehacek, *Sens. Actuators, B* **1999**, 57, 147.
- [15] M. Napari, T. N. Huq, R. L. Z. Hoye, J. L. MacManus-Driscoll, *InfoMat* **2021**, 3, 536.
- [16] Y. Kim, M. Kang, M. Lee, J. Kang, D. Kim, *Adv. Electron. Mater.* **2020**, 6, 2000189.
- [17] E. L. Ratcliff, J. Meyer, K. X. Steirer, A. Garcia, J. J. Berry, D. S. Ginley, D. C. Olson, A. Kahn, N. R. Armstrong, *Chem. Mater.* **2011**, 23, 4988.
- [18] R. Poulain, G. Lumbeck, J. Hunka, J. Proost, H. Savolainen, H. Idrissi, D. Schryvers, N. Gauquelin, A. Klein, *ACS Appl. Electron. Mater.* **2022**, 4, 2718.
- [19] D. Mariotti, T. Belmonte, J. Benedikt, T. Velusamy, G. Jain, V. Švrček, *Plasma Process. Polym.* **2016**, 13, 70.
- [20] D. Mariotti, R. M. Sankaran, *J. Phys. D: Appl. Phys.* **2010**, 43, 323001.
- [21] D. Mariotti, *Appl. Phys. Lett.* **2008**, 92, 1.
- [22] K. H. Becker, K. H. Schoenbach, J. G. Eden, *J. Phys. D: Appl. Phys.* **2006**, 39, R50.
- [23] Y. Shimizu, K. Koga, T. Sasaki, D. Mariotti, K. Terashima, N. Koshizaki, in *2007 Digest of papers Microprocesses and Nanotechnology*, IEEE, Kyoto, Japan **2007**, pp. 174–175.
- [24] D. Mariotti, H. Lindström, A. C. Bose, K. K. Ostrikov, *Nanotechnology* **2008**, 19, 495302.
- [25] K. E. Mackie, A. C. Pebley, M. M. Butala, J. Zhang, G. D. Stucky, M. J. Gordon, *Appl. Phys. Lett.* **2016**, 109, 033110.
- [26] P. A. Lin, A. Kumar, R. M. Sankaran, *Plasma Process. Polym.* **2012**, 9, 1184.
- [27] S. Chakrabarti, D. Carolan, B. Alessi, P. Maguire, V. Svrcek, D. Mariotti, *Nanoscale Adv.* **2019**, 1, 4915.
- [28] S.-Y. Han, D.-H. Lee, Y.-J. Chang, S.-O. Ryu, T.-J. Lee, C.-H. Chang, *J. Electrochem. Soc.* **2006**, 153, C382.
- [29] J. Keraudy, J. García Molleja, A. Ferrec, B. Corraze, M. Richard-Plouet, A. Goulet, P.-Y. Jouan, *Appl. Surf. Sci.* **2015**, 357, 838.
- [30] N. Kaur, E. Comini, D. Zappa, N. Poli, G. Sberveglieri, *Nanotechnology* **2016**, 27, 205701.
- [31] E. R. Beach, K. Shqau, S. E. Brown, S. J. Rozeveld, P. A. Morris, *Mater. Chem. Phys.* **2009**, 115, 371.
- [32] J. Mou, Y. Ren, J. Wang, C. Wang, Y. Zou, K. Lou, Z. Zheng, D. Zhang, *Microfluid. Nanofluidics* **2022**, 26, 25.
- [33] Y. Shimizu, A. C. Bose, D. Mariotti, T. Sasaki, K. Kirihara, T. Suzuki, K. Terashima, N. Koshizaki, *Jpn. J. Appl. Phys.* **2006**, 45, 8228.
- [34] A. C. Bose, Y. Shimizu, D. Mariotti, T. Sasaki, K. Terashima, N. Koshizaki, *Nanotechnology* **2006**, 17, 5976.
- [35] D. Mariotti, V. Švrček, D.-G. Kim, *Appl. Phys. Lett.* **2007**, 91, 183111.
- [36] D. Mariotti, K. Ostrikov, *J. Phys. D: Appl. Phys.* **2009**, 42, 092002.
- [37] G. Jain, M. Macias-Montero, T. Velusamy, P. Maguire, D. Mariotti, *Plasma Process. Polym.* **2017**, 14, 1700052.
- [38] A. U. Haq, S. Askari, A. McLister, S. Rawlinson, J. Davis, S. Chakrabarti, V. Svrcek, P. Maguire, P. Papakonstantinou, D. Mariotti, *Nat. Commun.* **2019**, 10, 817.
- [39] G. Jain, C. Rocks, P. Maguire, D. Mariotti, *Nanotechnology* **2020**, 31, 215707.
- [40] P. Brunet, R. J. McGlynn, B. Alessi, F. Smail, A. Boies, P. Maguire, D. Mariotti, *Nanoscale Adv.* **2021**, 3, 781.
- [41] Y. Shimizu, K. Kawaguchi, T. Sasaki, N. Koshizaki, *Appl. Phys. Lett.* **2009**, 94, 191504.
- [42] W. J. Duan, S. H. Lu, Z. L. Wu, Y. S. Wang, *J. Phys. Chem. C* **2012**, 116, 26043.
- [43] X. D. Zhou, W. Huebner, *Appl. Phys. Lett.* **2001**, 79, 3512.
- [44] A. N. Mansour, *Surf. Sci. Spectra* **1994**, 3, 231.
- [45] A. N. Mansour, C. A. Melendres, *Surf. Sci. Spectra* **1994**, 3, 247.
- [46] A. N. Mansour, C. A. Melendres, *Surf. Sci. Spectra* **1994**, 3, 263.
- [47] A. N. Mansour, C. A. Melendres, *Surf. Sci. Spectra* **1994**, 3, 271.
- [48] M. C. Biesinger, B. P. Payne, L. W. M. Lau, A. Gerson, R. S. C. Smart, *Surf. Interface Anal.* **2009**, 41, 324.
- [49] F. Ullrich, S. Hillebrandt, S. Hietzschold, V. Rohnacher, T. Marszalek, W. Kowalsky, R. Lovrincic, S. Beck, E. Mankel, A. Pucci, *ACS Appl. Energy Mater.* **2018**, 1, 3113.
- [50] H. A. E. Hagelin-Weaver, J. F. Weaver, G. B. Hoflund, G. N. Salaita, *J. Electron Spectros. Relat. Phenomena* **2004**, 134, 139.

- [51] E. R. Shaaban, M. A. Kaid, M. G. S. Ali, *J. Alloys Compd.* **2014**, *613*, 324.
- [52] P. Zhai, Q. Yi, J. Jian, H. Wang, P. Song, C. Dong, X. Lu, Y. Sun, J. Zhao, X. Dai, Y. Lou, H. Yang, G. Zou, *Chem. Commun.* **2014**, *50*, 1854.
- [53] H. Abdy, A. Aletayeb, M. Kolahdouz, E. A. Soleimani, *AIP Adv.* **2019**, *9*, 015216-1.
- [54] H. L. Yip, A. K. Y. Jen, *Energy Environ. Sci.* **2012**, *5*, 5994.
- [55] S. Hietzschold, S. Hillebrandt, F. Ullrich, J. Bombsch, V. Rohnacher, S. Ma, W. Liu, A. Köhn, W. Jaegermann, A. Pucci, W. Kowalsky, E. Mankel, S. Beck, R. Lovrincic, *ACS Appl. Mater. Interfaces* **2017**, *9*, 39821.
- [56] M. T. Greiner, M. G. Helander, Z.-B. Wang, W.-M. Tang, Z.-H. Lu, *J. Phys. Chem. C* **2010**, *114*, 19777.